Floquet engineering of twisted double bilayer graphene

Martin Rodriguez-Vega , 1,2,* Michael Vogl , 1,3,† and Gregory A. Fiete , 2,4

1 Department of Physics, The University of Texas at Austin, Austin, Texas 78712, USA

2 Department of Physics, Northeastern University, Boston, Massachusetts 02115, USA

3 Department of Physics, King Fahd University of Petroleum and Minerals, 31261 Dhahran, Saudi Arabia

4 Department of Physics, Massachusetts Institute of Technology, Cambridge, Massachusetts 02139, USA

(Received 15 June 2020; accepted 1 September 2020; published 25 September 2020)

Motivated by the recent experimental realization of twisted double bilayer graphene (TDBG) samples, we study, both analytically and numerically, the effects of circularly polarized light propagating in free space and confined in a waveguide on the band structure and topological properties of these systems. These two complementary Floquet protocols allow us to selectively tune different parameters of the system by varying the intensity and light frequency. For the drive protocol in free space, in the high-frequency regime, we find that in TDBG with AB/BA stacking, we can selectively close the zone-center quasienergy gaps around one valley while increasing the gaps near the opposite valley by tuning the parameters of the drive. In TDBG with AB/AB stacking, a similar effect can be obtained upon the application of a perpendicular static electric field. Furthermore, we study the topological properties of the driven system in different settings, provide accurate effective Floquet Hamiltonians, and show that relatively strong drives can generate flat bands. On the other hand, longitudinal light confined in a waveguide couples to the components of the interlayer hopping that are perpendicular to the TDBG sheet, allowing for selective engineering of the bandwidth of Floquet zone-center quasienergy bands without breaking the symmetries of the static system.

DOI: 10.1103/PhysRevResearch.2.033494

I. INTRODUCTION

Moiré superlattices have emerged as platforms to attain strongly correlated phases of matter by controlling the stacking configuration between the layers [1–3]. In twisted bilayer graphene (TBG) samples, examples include superconducting, Mott-insulating [4–8], and ferromagnetic states [9,10]. In twisted transition-metal dichalcogenide heterostructures (TMDs), evidence for moiré excitons has been reported [11–13]. More recently, twisted double bilayer graphene (TDBG) has emerged as a multi-flat-band system, exhibiting spin-polarized and correlated phases [14–20].

The plethora of strongly correlated phases available in moiré superlattices naturally invites the development of controllable mechanisms that would allow one to tune in and out of these phases. In equilibrium, hydrostatic pressure has been used to increase the tunneling strength and tune the magic angle in TBG [21–26]. On the other hand, out-of-equilibrium approaches, such as Floquet engineering [27–58], provide a more flexible and controllable route. Recently, the use of lasers at various frequencies has been proposed to engineer the Floquet band structure of graphene-based moiré superlattices.

Published by the American Physical Society under the terms of the Creative Commons Attribution 4.0 International license. Further distribution of this work must maintain attribution to the author(s) and the published article's title, journal citation, and DOI.

In the high-frequency regime, it has been shown that topological transitions can be induced in large twist angle TBG [59] and topological flat bands with nonzero Chern numbers can be induced in the ultraviolet regime [60]. In the near-infrared range, several flat bands can be generated [61]. In the low-frequency regime, Floquet drives can generate a large variety of broken-symmetry phases as revealed by effective Floquet Hamiltonians [62]. Finally, light confined to a waveguide provides a way to selectively increase or decrease the magic angle by driving in the low- or high-frequency regime [63].

Floquet engineering has also been proposed for the generation of valley polarized currents in graphene, TMDs, and van der Waals heterostructures [64–69] with applications in valleytronics [70,71]. An interesting effect with topological origin is the valley Hall effect [72–75], which has been experimentally observed in monolayer TMDs illuminated with circularly polarized light [76] and graphene hexagonal boron nitride heterostructures [77]. Also, in TMDs, exciton level selective tuning using intense circularly polarized light has been demonstrated [78] and the valley Bloch-Siegert shift has been observed [79]. Furthermore, in bilayer graphene in the presence of a perpendicular electric field, valley topological transport has been reported [80,81]. New flexible and controllable platforms for the manipulation of the valley degree of freedom are highly desirable for information processing.

In this work we consider TDBG in the AB/AB and AB/BA configurations irradiated by circularly polarized light in free space and confined to a waveguide. We show by deriving effective Floquet Hamiltonians and by numerical calculations that light in free space can induce transitions from a trivial or valley Chern insulator (depending on the stacking

^{*}rodriguezvega@utexas.edu

[†]ssss133@googlemail.com

configuration) into a Chern insulator. Furthermore, in the presence of a transverse electric field, driven AB/AB TDBG allows the quasienergy gaps at the K and K' valleys to be selectively tuned by varying the direction of the static electric field and by modulating the amplitude and frequency of the driving laser. For AB/BA TDBG, we find that the quasienergy gaps can be tuned selectively even without an applied electric field. The flexibility of the quasienergy band structure near the Floquet zone center can be used to generate valley polarized currents in TDBG, independent of the stacking configuration. On the other hand, using light confined to a waveguide allows us to dynamically tune the component of the tunneling perpendicular to the plane without breaking the symmetries of the static system.

The rest of the paper is organized as follows. In Sec. II we describe static TDBG and the notation we adopt throughout

the paper. In Sec. III we consider TDBG driven by circularly polarized light in free space. We consider both high- and intermediate-frequency regimes and describe the effects on the band structure and the topological aspects in each regime. In Sec. IV we consider a drive protocol using longitudinal vector potentials, allowed inside a waveguide, and discuss the effects on the quasienergies. In Sec. V we comment on the experimental drive parameters necessary to observe the effects discussed previously. In Sec. VI we present a summary and our conclusions.

II. STATIC SYSTEM

In the continuum limit, the static Hamiltonian for TDBG near the K point with AB/AB (s = s' = 1) [AB/BA (s = -s' = 1)] stacking patterns is given by [15–17]

$$H_{ss'}(\mathbf{k}, \mathbf{x}) = \tau_u \otimes h_s(-\theta/2, \mathbf{k} - \kappa_-) + \tau_d \otimes h_{s'}(\theta/2, \mathbf{k} - \kappa_+) + \tau^+ \otimes \lambda^- \otimes T(\mathbf{x}) + \tau^- \otimes \lambda^+ \otimes T^{\dagger}(\mathbf{x}), \tag{1}$$

where $\tau_u = (\mathbb{1} + \tau_3)/2$, $\tau_d = (\mathbb{1} - \tau_3)/2$, $\tau_{\pm} = (\tau_1 \pm i\tau_2)/2$, and τ_i and λ_i are Pauli matrices in the top/bottom bilayer and layer space, respectively. Here σ_k are Pauli matrices or identity operators in pseudospin space. The bilayer graphene Hamiltonian is given by [82]

$$h_s(\theta, \mathbf{k}) = \begin{pmatrix} \Delta_1 + \delta_s^- & \gamma_0 f(R_\theta \mathbf{k}) & t_s(\mathbf{k}) \\ \gamma_0 f^*(R_\theta \mathbf{k}) & \Delta_1 + \delta_s^+ & \\ \hline t_s^{\dagger}(\mathbf{k}) & \Delta_2 + \delta_s^+ & \gamma_0 f(R_\theta \mathbf{k}) \\ \hline t_s^{\dagger}(\mathbf{k}) & \gamma_0 f^*(R_\theta \mathbf{k}) & \Delta_2 + \delta_s^- \end{pmatrix},$$
(2)

with the tunneling matrix

$$t_{+}(\mathbf{k}) = \begin{pmatrix} -\gamma_{4} f(R_{\theta} \mathbf{k}) & -\gamma_{3} f^{*}(R_{\theta} \mathbf{k}) \\ \gamma_{1} & -\gamma_{4} f(R_{\theta} \mathbf{k}) \end{pmatrix}$$
(3)

and $t_-(k) = t_+^{\dagger}(k)$. Each diagonal block in Eq. (2) corresponds to the top and bottom layers of each bilayer unit, $f(k) = k_x - ik_y$ describes the intralayer hopping between nearest-neighbor sites, and $\gamma_0 = v_F/a_0$ in natural units ($\hbar = c = e = 1$). Here Δ_i corresponds to a potential on graphene layer i, which will describe the effect of an applied electric field perpendicular to the sample surface. Finally, $\delta_s^{\pm} = \delta(1 \pm s)/2$ is a stacking-and layer-dependent gap [82].

The off-diagonal blocks $t_s(\mathbf{k})$ describe the tunneling processes within each bilayer unit [82], including contributions from vertical tunneling γ_1 and next-nearest-neighbor tunneling γ_3 and γ_4 ; γ_3 leads to trigonal warping and γ_4 to particle-hole symmetry breaking. The tunneling sector also depends on the bilayer stacking configuration s.

The interlayer hopping matrix

$$T(x) = \sum_{i=-1}^{1} e^{-iQ_i \cdot x} T_i,$$
 (4)

with

$$T_i = w_0 \mathbb{1}_2 + w_1 \left[\cos \left(\frac{2\pi i}{3} \right) \sigma_1 + \sin \left(\frac{2\pi i}{3} \right) \sigma_2 \right],$$

describes tunneling between the two graphene bilayers, where $Q_0 = (0, 0)$ and $Q_{\pm 1} = k_{\theta}(\pm \sqrt{3}/2, 3/2)$ are the reciprocal

lattice vectors. We neglect direct tunneling contributions between layers that are not adjacent to one another, as indicated by the structure $\tau^+ \otimes \lambda^- \otimes T(x)$. The parameter w_1 in the tunneling term models relaxation effects, since the AB and BA configurations within each bilayer units are energetically preferred over the AA configuration [83,84]. Throughout this work, we set the parameters $\gamma_0 = v_F/a_0 = 2.36$ eV, $a_0 = 2.46$ Å, $w_0 = 100$ meV, $w_1 = 120$ meV, $\gamma_3 = 283$ meV, $\gamma_4 = 138$ meV, and $\delta = 15$ meV unless otherwise explicitly stated. In Fig. 1(a), we show a sketch of the system we consider, and in panel (b) the Moiré Brillouin zone (MBZ) and band structure for twisted double bilayer graphene near the K point for $\theta = 1.05^{\circ}$.

The Hamiltonian near the K' valley can be obtained by applying a time-reversal operation \mathcal{T} to the Hamiltonian at the K valley [85]. Before studying the time-dependent case it is worthwhile to summarize various symmetry properties of static TDBG. In addition to time-reversal symmetry \mathcal{T} , AB/AB TDBG possesses C_{3z} rotational symmetry and mirror symmetry $M_x: y, k_y \rightarrow -y, -k_y$ in the absence of an applied static electric field. The AB/BA TDBG possesses C_{3z} , mirror symmetry $M_y: x, k_x \rightarrow -x, -k_x$ (which switches the valleys), and $M_y\mathcal{T}$ [16,17,20].

In addition, TDBG displays topological properties captured by the Chern number, which is defined by $C = \sum_{n \in \text{occ}} C_n$, with the band Chern number

$$C_n = \frac{1}{2\pi} \int_{\text{MBZ}} F_n(\mathbf{k}) d\mathbf{k}, \tag{5}$$

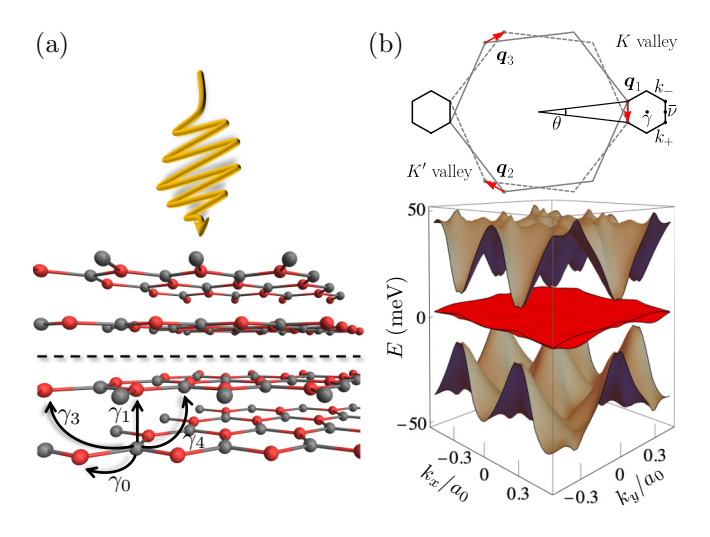


FIG. 1. (a) Sketch of double bilayer graphene irradiated by circularly polarized light. The black arrows indicate the various tunneling processes within each bilayer. The dashed black line represents the twist. (b) Moiré Brillouin zone (MBZ) and band structure for twisted double bilayer graphene near the K point neglecting $\gamma_{3/4}$. The parameters are $w_0 = 100$ meV, $w_1 = 120$ meV, and $\theta = 1.05^{\circ}$.

where $F_n(\mathbf{k}) = [\nabla \times \mathcal{A}_n(\mathbf{k})]_z$ is the Berry curvature, $\mathcal{A}_n(\mathbf{k}) = -i \langle u_n(\mathbf{k}) | \partial_k | u_n(\mathbf{k}) \rangle$ the Berry connection, and $|u_n(\mathbf{k})\rangle$ the eigenstates of $H_{ss'}(\mathbf{k}, \mathbf{x})$ defined on a plane-wave basis. Time-reversal symmetry implies that the Chern numbers for each valley are opposite to each other for a given band n, $C_n^K = -C_n^{K'}$. In the absence of a potential difference $\Delta_i = 0$, the M_y symmetry of AB/AB TDBG implies $C_n^{K/K'} = 0$ for each band n [17], since it does not interchange the valleys. For example, by explicit evaluation of Eq. (5) near K, we find that AB/AB TDBG with $\gamma_{3/4} = 0$ has trivial Chern numbers $C_a^K = C_b^K = C_c^K = 0$ at gaps δE_i , where i = a, b, c labels the gaps as shown in Fig. 2. On the other hand, AB/BA TDBG has nontrivial Chern numbers $C_a^K = -1$, $C_b^K = 2$, and $C_c^K = 1$ even for $\Delta_i = 0$. At the K'

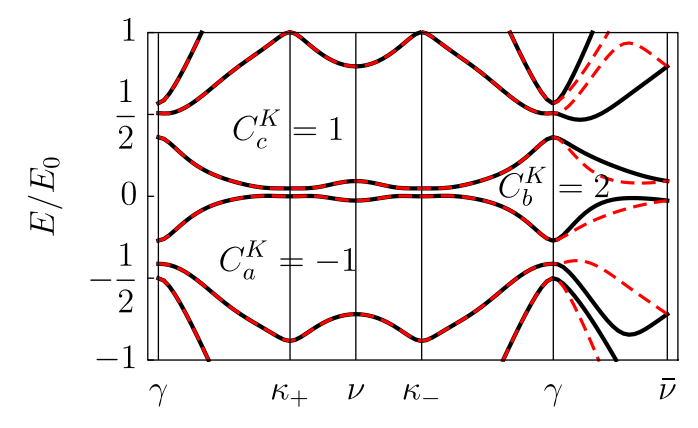


FIG. 2. The AB/BA TDBG band structure for $\theta=1.4^{\circ}$, $\Delta=0$, and $\gamma_{3/4}=0$ along a high-symmetry path in the MBZ. The black solid (red dashed) lines correspond to the spectrum near the K (K') point. The Chern numbers in the gaps labeled a, b, and c are indicated for the K point. Time-reversal symmetry imposes $C^{K'}=-C^K$. The energy scale is $E_0=100$ meV.

point, we find $C_a^{K'} = 1$, $C_b^{K'} = -2$, and $C_c^{K'} = -1$, as required by time-reversal symmetry, placing AB/BA TDBG in a Hall valley insulating phase.

In the next section we will study the effect of circularly polarized light on TDBG.

III. DRIVEN SYSTEM IN FREE SPACE

In this section we consider the effect of circularly polarized light in free space at normal incidence to the TDBG surface. The time-dependent Hamiltonian near the K point is given by $H_{ss'}(t) \equiv H_{ss'}(k(t), x)$,

$$H_{ss'}(\mathbf{k}(t), \mathbf{x}) = \tau_u \otimes h_s(-\theta/2, \mathbf{k}(t) - \kappa_-)$$

$$+ \tau_d \otimes h_{s'}(\theta/2, \mathbf{k}(t) - \kappa_+)$$

$$+ \tau^+ \otimes \lambda^- \otimes T(\mathbf{x}) + \tau^- \otimes \lambda^+ \otimes T^{\dagger}(\mathbf{x}),$$
(6)

and $k_x(t) = k_x - A\cos(\Omega t)$ and $k_y(t) = k_y - A\sin(\Omega t)$. Here we used a minimal coupling procedure that is valid for not-too-strong couplings to the electromagnetic field [86]. The vector potential enters in the same way near both the K and K' points. The interbilayer tunneling sector has, in principle, contributions parallel to the surface that could couple to the normally incident circularly polarized light. However, the orbital overlap decays exponentially away from sites that sit on top of each other in a twisted sample [1]. The time-dependent Hamiltonian (6) satisfies $H_{ss'}(t+2\pi/\Omega)=H_{ss'}(t)$. Therefore, we employ Floquet theory to write the wave functions as $|\psi(t)\rangle=e^{i\epsilon t}|\phi(t)\rangle$, where $|\phi(t+2\pi/\Omega)\rangle=|\phi(t)\rangle$ are the steady states and ϵ is the quasienergies which satisfy the Floquet Schrödinger equation

$$[H_{ss'}(t) - i\partial_t]|\phi(t)\rangle = \epsilon |\phi(t)\rangle. \tag{7}$$

In the extended-space picture [28,37,87], $|\phi(t)\rangle = \sum_n e^{in\Omega t} |\phi_n\rangle$. An expansion of the operator $[H_{ss'}(t) - i\partial_t]$ in modes $e^{in\Omega t}$ leads to $\sum_m (H_{ss'}^{(n-m)} + \delta_{n,m}\Omega m) |\phi_m\rangle = \epsilon |\phi_n\rangle$, where $H_{ss'}^{(n)} = \int_0^{2\pi} d\tau/(2\pi) H_{ss'}(\tau) e^{-i\tau n}$. In the next two sections we consider the effects of the drives in the high- and intermediate-frequency regimes, respectively.

A. High frequency

In the high-frequency regime, we employ the Van Vleck expansion [28] to obtain an effective Floquet Hamiltonian $H_{\text{VV}}^{ss'} = H_{ss'}^{(0)} + \delta H_{ss',\text{VV}}$, where $H_{ss'}^{(0)}$ is the Hamiltonian averaged over one drive period and

$$\delta H_{ss',VV} = -\left(\Delta_{VV} - \Delta_{VV}^{(3)}\right) \mathbb{1} \otimes \mathbb{1} \otimes \sigma_3 - \left(\Delta_{VV}^{(4)} - \Delta_{VV}^{(3)}\right)$$

$$\times (s\tau^u \otimes \lambda_3 \otimes \mathbb{1} + s'\tau^d \otimes \lambda_3 \otimes \mathbb{1}), \tag{8}$$

where $\Delta_{\rm VV} = \xi(v_F A)^2/\Omega$, $\Delta_{\rm VV}^{(4)} = \xi(v_4 A)^2/\Omega$, and $\Delta_{\rm VV}^{(3)} = \xi(v_3 A)^2/2\Omega$, with $\xi = 1$ ($\xi = -1$) near the K (K') valley. The simplicity of the high-frequency regime Van Vleck expansion allows us to also retain the effects of $\gamma_{3,4}$, which are harder to capture using more sophisticated intermediate-frequency-regime methods introduced in later sections.

The gap $\Delta_{\rm VV}$ is generated due to the effect that light has on the hopping in each graphene layer, which is captured by the component $\mathbb{1} \otimes \mathbb{1} \otimes \{\sigma \cdot [k - A(t)]\}$ in the time-dependent

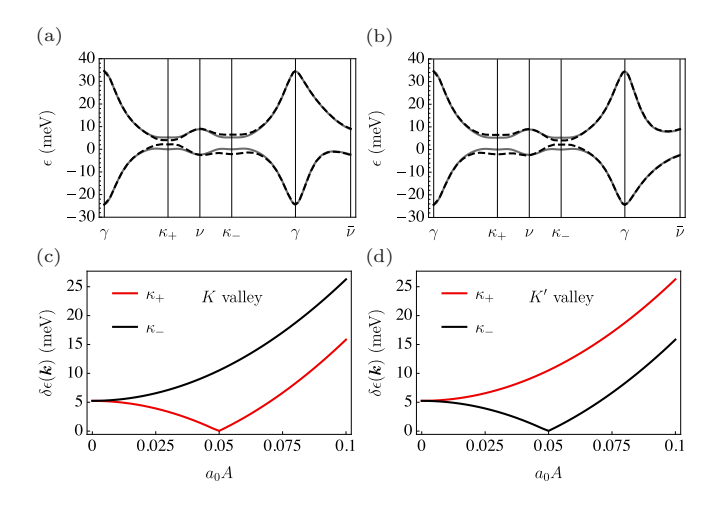


FIG. 3. The AB/AB TDBG quasienergies near (a) the K point and (b) the K' point along a high-symmetry path in the MBZ for $\theta=1.4^\circ$, $\Omega/W=2$, and $a_0A=0.04$. The gray curves correspond to the equilibrium energies. Also shown is the quasienergy gap for κ_\pm as a function of the driving strength a_0A for $\Omega/W=2$ (c) at the K valley, where κ_+ closes at $a_0A\approx0.05$, and (d) at the K' valley, where κ_- closes at the same driving strength.

Hamiltonian. It breaks both time-reversal \mathcal{T} and mirror symmetries $(M_x \text{ for } AB/AB \text{ and } M_y \text{ for } AB/BA)$ and is stacking independent. The gaps $\Delta_{VV}^{(3,4)}$ are induced by the effect that light has on interlayer hoppings that have components in the plane. Specifically, these interlayer hoppings are within the top and bottom bilayers and are captured by the terms $\{\tau^u \otimes$ $\lambda^+ \otimes t_s[\boldsymbol{p} - \boldsymbol{A}(t)] + \tau^d \otimes \lambda^+ \otimes t_{s'}[\boldsymbol{p} - \boldsymbol{A}(t)]$ + H.c. in the time-dependent Hamiltonian. Specifically, $\Delta_{VV}^{(4)}$ is induced by hopping between equivalent lattice sites on opposite layers. It constitutes a potential difference between the graphene layers in each bilayer unit and breaks both time-reversal and mirror symmetries in both stacking configurations. In contrast, $\Delta_{VV}^{(3)}$ is caused by hoppings between inequivalent sublattices on opposite layers. It has two components. The first one is independent of the stacking configuration and acts as Δ_{VV} . The second component depends on the stacking configuration (AB/AB or AB/BA) and acts as $\Delta_{VV}^{(4)}$. Next we will review the effect of these dynamically induced terms on the topological properties of TDBG.

In equilibrium, AB/AB TDBG is a trivial insulator for $\Delta_i =$ 0. The finite Δ_{VV} induced by circularly polarized light leads to a transition into a Chern insulator with Floquet topological bands. For example, consider the case $\theta = 1.4^{\circ}$, $\gamma_{3/4} = 0$, and $\Omega/W = 2$, with $W = v_F/a_0$. In Figs. 3(a) and 3(b) we show the quasienergy spectrum near the Floquet zone center ϵ/Ω = 0 at the K and K' valleys, respectively. The effect of light at the κ_{\pm} near each valley is the opposite of each other. In Figs. 3(c) and 3(d) we show the evolution of the quasienergy gap at κ_+ as a function of the drive strength obtained numerically by diagonalizing the Hamiltonian in the Floquet extended space. When the gap closes at κ_+ for $a_0 A \approx 0.05$ and then opens again, the band Chern number changes from zero to $C_{n=-1}^{K} = -2$ for the lower Floquet zone-center quasienergy band (labeled as n = -1) and $C_{n=1}^{K} = 2$ for the higher quasienergy band. This can be understood from the sum of the contributions of the Berry curvature from the four Dirac cones composing TDBG

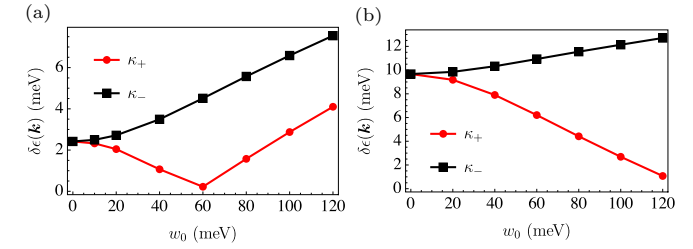


FIG. 4. The AB/AB TDBG quasienergy gaps at κ_{\pm} near the K valley for $\theta=1.4^{\circ}$, $\Omega/W=2$, and (a) $a_0A=0.03$ and (b) $a_0A=0.06$ as a function of the tunneling between the bilayer units. We set $w_0=w_1$ in this case.

near the K valley. At the K' valley, we find $C_n^{K'} = C_n^K$, since the restrictions from time-reversal symmetry are lifted. The asymmetric behavior of the gaps at κ_\pm arises because the hybridization of the twisted bilayers breaks inversion symmetry and there is no C_{2z} rotational symmetry as in TDG, leading to a generic gapped state in the absence of a drive. Upon the application of the drive, the states at κ_\pm evolve in time in distinct manners resulting in the structure of $\Delta_{\rm VV}$ in the effective Floquet Hamiltonian. In Fig. 4 we show the evolution of the gap at κ_\pm as a function of the tunneling amplitude between the twisted bilayers for drive strengths $a_0A=0.03$ and 0.06 (below and above the light-induced transition for the nominal values $w_0=100$ meV and $w_1=120$ meV). For fully decoupled layers ($w_0=w_1=0$), the gaps are symmetric.

After discussing the Chern number, we recall that while it is a measurable quantity [88,89], it is not what determines the number of edge states. Rather, in Floquet systems the bulk-edge correspondence is determined by the winding number $\mathcal{W}[\mathcal{U}_{\varepsilon}]$, defined at a quasienergy ε inside a gap [90], where

$$W[\mathcal{U}] = \frac{1}{8\pi^2} \int dt \, d\mathbf{k} \, \text{Tr} \left(\mathcal{U}^{-1} \partial_t \mathcal{U} \left[\mathcal{U}^{-1} \partial_{k_x} \mathcal{U}, \mathcal{U}^{-1} \partial_{k_y} \mathcal{U} \right] \right)$$
(9)

and $\mathcal{U}_{\varepsilon}$ is a modified time-evolution operator [90]. Here we calculate \mathcal{W} via the truncated Floquet Hamiltonian in the extended space [90]. For the AB/AB TDBG case above, we find $\mathcal{W}_a^K = 0$, $\mathcal{W}_b^K = -2$, $\mathcal{W}_c^K = 0$, and $\mathcal{W}^{K'} = \mathcal{W}^K$ at the three gaps considered around the quasienergy bands shown in Figs. 3(a) and 3(b).

Now let us consider the AB/BA configuration for TDBG with $\Delta_i=0$. In contrast to AB/BA TDBG, AB/BA TDBG is a valley Chern insulator at equilibrium. The energies and Chern numbers inside the gaps are shown in Fig. 2. As for the case of AB/AB TDBG, circularly polarized light leads to a transition into a Chern insulating phase with finite Floquet band Chern and winding numbers. However, in this configuration, the behavior of the κ_\pm gaps is different: At the K valley, both κ_\pm gaps close at drive amplitude $a_0A \approx 0.058$ for $\Omega/W=2$, while the κ_\pm gaps near the K' valley increase monotonically with a_0A (see Fig. 5). This selective gap engineering could be employed to generate valley-polarized currents in AB/BA TDBG; however, the calculation of valley-polarized current in specific devices is beyond the scope of our work.

As for the topological properties, the Floquet band Chern numbers switch after the transition: $C_{n=-2}^K = -1$, $C_{n=-1}^K = -1$, $C_{n=1}^K = 3$, and $C_{n=2}^K = -1$. The winding numbers inside

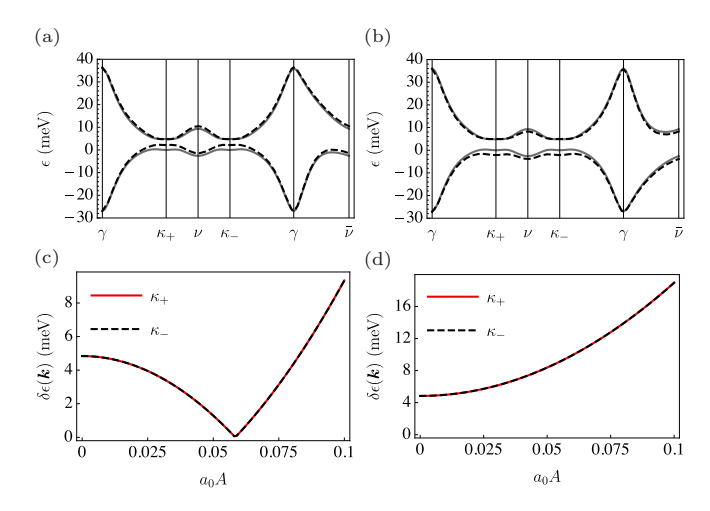


FIG. 5. The AB/BA TDBG quasienergies near (a) the K point and (b) the K' point along a high-symmetry path in the MBZ. The parameters are the same as in Fig. 3. The gray curves correspond to the equilibrium energies. Also shown is the quasienergy gap for κ_{\pm} as a function of the driving strength a_0A for $\Omega/W=2$ at (c) the K point and (d) the K' point.

the gaps are $\mathcal{W}_a^K = -1$, $\mathcal{W}_b^K = -2$, and $\mathcal{W}_c^K = 1$, with a change from gap to gap in correspondence with the Floquet band Chern numbers.

Since the gaps do not close at the K' point in the range of parameters we considered, the band Chern numbers remain the same as in the static case: $C_{n=-2}^{K'}=1$, $C_{n=-1}^{K'}=-3$, $C_{n=1}^{K'}=1$, and $C_{n=2}^{K'}=1$. For the winding numbers, we obtain $W_a^{K'}=1$, $W_b^{K'}=-2$, and $W_c^{K'}=-1$.

1. Applied static electric field

So far, we have restricted our analysis to $\Delta_i = 0$, which corresponds to no potential difference between the layers (apart from δ_s^{\pm}). Now we consider AB/AB TDBG in the presence of an applied perpendicular static electric field, which leads to a potential difference between the layers. In experiments, dual-gated bilayer graphene devices have been realized for optoelectronic applications using semitransparent top gates [91,92].

Here we set $\Delta_4 = -\Delta_1$, $\Delta_3 = -\Delta_2$, $\Delta_1 = 3U/2$, and $\Delta_2 = U/2$, with U the potential difference. In equilibrium, the transverse electric field places AB/AB TDBG in a valley Chern insulating regime. For U = 10 meV, we find in the static case the band Chern numbers $C_{-1}^{K} = -2$ and $C_{1}^{K} =$ 2 and corresponding total Chern numbers inside the gaps $C_a^K = 0$, $C_b^K = -2$, and $C_c^K = 0$. At the K' valley, we find $C_n^{K'} = -C_n^{K}$, as imposed by time-reversal symmetry. When one drives the system, the gaps at the Floquet zone center are renormalized. In Fig. 6(a) we plot the evolution of the quasienergy gaps at the κ_{\pm} points as a function of the drive amplitude. Near the K valley, the quasienergy differences at κ_{\pm} increase monotonically with a_0A . Since the gap remains open for the driving parameters considered, the Chern and winding numbers do not change. In contrast, at the K' point, the quasienergy differences decrease starting from different values in the vanishing drive strength limit, leading to a gap

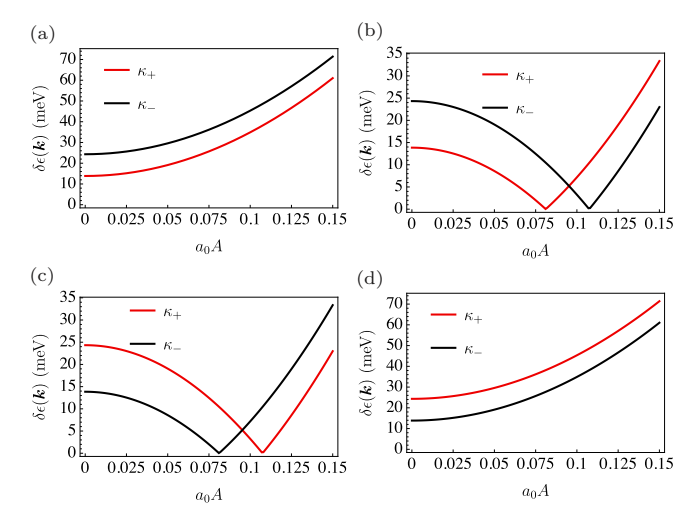


FIG. 6. The AB/AB TDBG quasienergy gap near (a) the K valley and (b) the K' valley at κ_{\pm} for U=10 meV. (c) and (d) Results for U=-10 meV. The rest of the parameters are the same as in Fig. 3.

closing at κ_+ for $a_0 A \approx 0.08$, followed by a closing at κ_- for $a_0 A \approx 0.107$. At the first quasienergy gap closing, the winding number changes from $\mathcal{W}_b^{K'} = 2$ to $\mathcal{W}_b^{K'} = 0$ and after the second gap closing to $\mathcal{W}_b^{K'} = -2$. The gap behavior at the K and K' valleys can be switched by changing the sign of the applied electric field, as shown in Figs. 6(c) and 6(d).

2. Trigonal warping and particle-hole symmetry-breaking terms

The structure of the Van Vleck Hamiltonian (8) shows that trigonal warping (the γ_3 term in the bilayer graphene tunneling sector) induces a small correction to the gap Δ_{VV} , since $\Delta_{VV}^{(3)}/\Delta_{VV}\approx 0.014$, independently of the frequency and amplitude of the drive. However, the effect in the static energies is not negligible.

Combined particle-hole asymmetry (γ_4) and trigonal warping effects induce a stacking-dependent gap. For AB/AB stacking s=s'=1, the gap has the structure $(\Delta_{\text{VV}}^{(4)}-\Delta_{\text{VV}}^{(3)})\mathbb{1}\otimes\lambda_3\otimes\mathbb{1}$, which constitutes a potential difference between the graphene composing each bilayer, with $|(\Delta_{\text{VV}}^{(4)}-\Delta_{\text{VV}}^{(3)})/\Delta_{\text{VV}}|\approx 0.01$. For AB/BA stacking s=-s'=1, the gap has the form $(\Delta_{\text{VV}}^{(4)}-\Delta_{\text{VV}}^{(3)})\tau_3\otimes\lambda_3\otimes\mathbb{1}$. In general, these terms can renormalize the topological transition points. For example, in Fig. 7 we plot the quasienergy gap at the κ_\pm points as a function of the driving strength a_0A for two frequencies

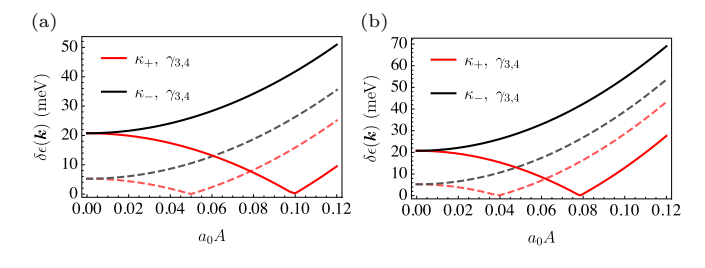


FIG. 7. The AB/AB TDBG quasienergy gap near the K valley at κ_{\pm} $\gamma_{3,4}=0$ (dashed curves) and $\gamma_{3,4}\neq 0$ (solid lines) as a function of the driving strength for (a) $\Omega/W=2$ and (b) $\Omega/W=1.25$.

in the high-frequency regime. Therefore, although the static energies can be significantly modified by $\gamma_{3,4} \neq 0$, Floquet drives can be used to manipulate the gap structure.

In this section we restricted the discussion to high-frequency and weak drives. In the next section we will derive an effective Floquet Hamiltonian valid for intermediate frequencies and intermediate drive strengths. We will show in particular that in this regime we can generate Floquet flat bands, which are impaired by trigonal warping and particle-hole symmetry-breaking effects.

B. Intermediate frequency

In the intermediate-frequency and intermediate-drive-strength regime, we obtain an effective Hamiltonian by performing a modified rotating frame transformation [62] and taking an average over one period (see the Appendix for details). In this work we define the intermediate-frequency regime as $\Omega > W + W_f$, where W_f corresponds to the bandwidth of the bands at the center of the spectrum we are interested in studying. Within this frequency regime, we can describe the system accurately down to frequencies lower than a high-frequency expansion, as we will discuss in this section. For our analytical results, we neglect the effect of next-to-nearest-neighbor hopping within each bilayer unit ($\gamma_3 = \gamma_4 = 0$), but we will discuss them numerically. Then the effective Floquet Hamiltonian is given by

$$H_F^{ss'} = R^{\dagger} (\bar{H}_{ss'} + \delta H_F) R, \tag{10}$$

where R is a twist-angle-dependent unitary transformation (see the Appendix for the explicit expression) and $\delta H_F = \Delta_F \mathbb{1} \otimes \mathbb{1} \otimes \sigma_3$, with $\Delta_F = AJ_1(2\sqrt{2}A/\Omega)/\sqrt{2}$, where $J_n(z)$ corresponds to the nth Bessel function of the first kind. As in the high-frequency regime, δH_F is independent of the AB/AB or AB/BA stacking configuration. Here $\bar{H}_{ss'}$ is given by

$$\begin{split} \bar{H}_{ss'}(\boldsymbol{k}, \boldsymbol{x}) &= \tau_u \otimes \tilde{h}_s(-\theta/2, \boldsymbol{k} - \kappa_-) \\ &+ \tau_d \otimes \tilde{h}_{s'}(\theta/2, \boldsymbol{k} - \kappa_+) \\ &+ \tau^+ \otimes \lambda^- \otimes \tilde{T}(\boldsymbol{x}) + \tau^- \otimes \lambda^+ \tilde{\otimes} T^{\dagger}(\boldsymbol{x}), \end{split} \tag{11}$$

where

$$\tilde{h}_{s}(\theta, \mathbf{k}) = \begin{pmatrix} \Delta_{1} + \tilde{\delta}_{s}^{-} & \tilde{\gamma}_{0} f(R_{\theta} \mathbf{k}) & \tilde{t}_{s} \\ \tilde{\gamma}_{0} f^{*}(R_{\theta} \mathbf{k}) & \Delta_{1} + \tilde{\delta}_{s}^{+} & \\ & & \Delta_{2} + \tilde{\delta}_{s}^{+} & \tilde{\gamma}_{0} f(R_{\theta} \mathbf{k}) \\ \tilde{t}_{s}^{\dagger} & & \tilde{\gamma}_{0} f^{*}(R_{\theta} \mathbf{k}) & \Delta_{2} + \tilde{\delta}_{s}^{-} \end{pmatrix},$$

$$(12)$$

with $\tilde{\gamma}_0 = J_0(2A/\Omega)\gamma_0 = J_0(2A/\Omega)v_F/a_0$, which is interpreted as a reduction of the Fermi velocity. The layerand stacking-dependent gap $\tilde{\delta}_s^{\pm} = \delta J_0(2\sqrt{2}A/\Omega)(1\pm s)/2$ is suppressed and the tunneling is now given by $\tilde{t}_s = \gamma_1 J_0(2A/\Omega)(\sigma_1 - is\sigma_2)/2$. None of these effects are captured in a leading-order Van Vleck expansion and it is challenging to capture the functional form simply by computing higherorder terms. The position-dependent interlayer coupling for

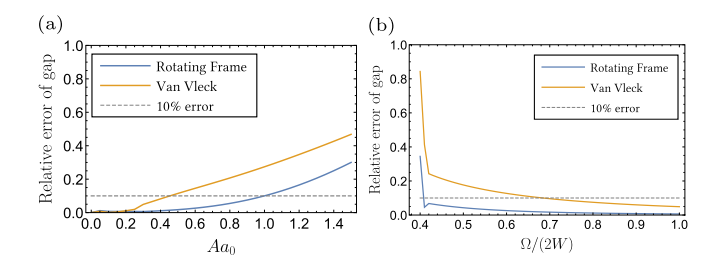


FIG. 8. Relative error of the quasienergy gap at the κ_+ point in the MBZ for $\delta=0$ meV as a function of (a) the driving strength for $\Omega/W=2$ and (b) the frequency for $a_0A=0.3$. In the whole range considered, the rotating frame effective Hamiltonian provides a more accurate approximation to the exact gap.

the two center graphene layers renormalizes to

$$\tilde{T}(\mathbf{x}) = \sum_{n=-1}^{1} e^{-i\mathbf{Q}_{n} \cdot \mathbf{x}} (\tilde{T}_{n} - i\omega_{\theta}\sigma_{3}),$$

$$\tilde{T}_{n} = \tilde{\omega}_{0} \mathbb{1}_{2} + \tilde{\omega}_{1} \left[\cos \left(\frac{2\pi n}{3} \right) \sigma_{1} + \sin \left(\frac{2\pi n}{3} \right) \sigma_{2} \right], \quad (13)$$

where

$$\tilde{\omega}_1 = J_0(2A/\Omega)\omega_1,$$

$$\tilde{\omega}_0 = \omega_0 + \sin^2(\theta/2) \left[J_0 \left(\frac{2\sqrt{2}A}{\Omega} \right) - 1 \right] \omega_0$$
 (14)

are renormalized interlayer couplings and a new angle-dependent coupling

$$\omega_{\theta} = \frac{1}{2}\sin(\theta) \left[J_0 \left(\frac{2\sqrt{2}A}{\Omega} \right) - 1 \right] \omega_0 \tag{15}$$

has been introduced that is absent from the equilibrium case.

As can be deduced from Fig. 8, this effective Hamiltonian is accurate up to frequency and driving strength regimes where the Van Vleck approximation breaks down. In particular, for a driving frequency $\Omega/W = 2$ one can describe gaps with errors below 10% up to driving strengths $a_0A \approx 1$, in contrast to the Van Vleck approximation, which only manages to do so until $a_0A \approx 0.45$. Therefore, the implementation of an improved transformation in a rotating frame can enhance the range of validity of effective Floquet Hamiltonians when it comes to driving strengths. A similar observation can be made if one keeps the driving strength fixed (in our case $a_0A = 0.3$) and varies the frequency. The rotating frame Hamiltonian here describes gaps with an error of less than 10% for frequencies as low as $\Omega/(2W) = 0.45$, while the Van Vleck expansion has the same level of accuracy only up to $\Omega/(2W) = 0.75$. Therefore, the approach allows one to reach into an intermediate-strength and intermediatefrequency regime, while the Van Vleck expansion is restricted to large frequencies and weak coupling. This type of effective Hamiltonian could make it easier to simultaneously describe the effects of circularly polarized light for a wide range of driving protocols and computationally challenging additional effects such as disorder.

Finally, in Figs. 9(a) and 9(b) we plot the quasienergy spectrum around the Floquet zone center and along a high-symmetry path in the MBZ for drive frequency $\Omega/W = 1.05$

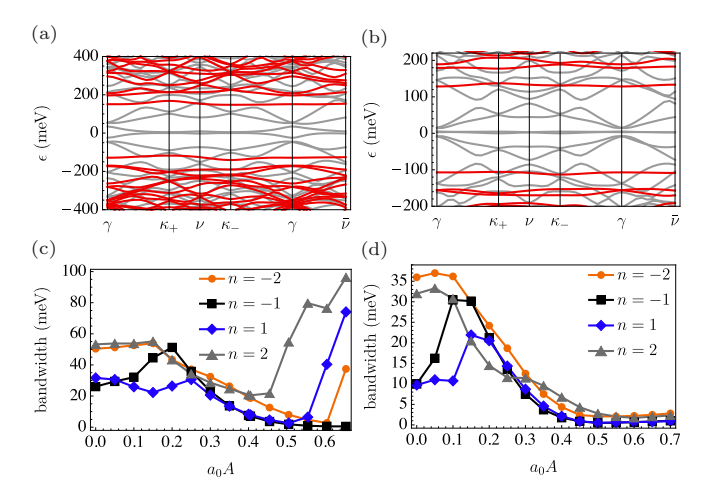


FIG. 9. (a) The AB/AB TDBG quasienergies near the K valley along a high-symmetry path in the MBZ for $\theta=1.4^\circ$, $\Delta_i=0$, $\Omega/W=1.05$, and $a_0A=0.3$. The gray curves correspond the equilibrium energies. (b) Case $\theta=1.05^\circ$ for the same drive parameters as in (a). Also shown is the bandwidth of the Floquet bands nearest (|n|=1) and next to nearest (|n|=2) the Floquet zone center for (c) $\theta=1.4^\circ$ and (d) $\theta=1.05^\circ$ as a function of the drive strength.

and drive strength $a_0A = 0.3$. We included the effects of trigonal warping and particle-hole asymmetry. In this case, the drive induces a large gap between the central quasienergy bands and modifies the bandwidth of these and the adjacent bands. To quantify the degree to which the quasienergy bands are flattened, in Figs. 9(c) and 9(d) we show the bandwidth of the Floquet bands nearest (|n| = 1) and next to nearest (|n| = 2) the Floquet zone center as a function of a_0A . The laser properties can be tuned such that the quasienergy bandwidth reaches a minimum. Therefore, stronger drives can generate Floquet flat bands, even in the presence of trigonal warping and particle-hole asymmetry, which in equilibrium tend to endow the bands with significant dispersion [17].

To conclude this section, we discuss the heating in the intermediate-frequency regime when interactions are present. In the high-frequency regime, the laser drive is not in resonance with transitions and the heating can take exponentially long times to set in [33,93]. When the drive frequency is in resonance, one needs to take into account relaxation processes to fully describe the system, such as coupling with phonons which can act as a reservoir [94–96]. Interestingly, a recent study on dissipative Floquet systems has shown that for resonant and strong-enough drives, Floquet states can develop if the decoherence time is shorter than the period of the drive [97]. Extensions of this work to consider such dissipative effects are beyond the scope of the present work.

In the next section we will consider an alternative Floquet drive protocol, which directly modifies the interlayer coupling, in contrast with the Floquet protocol considered in this section.

IV. DRIVEN SYSTEM IN A WAVEGUIDE

In this section we consider a complementary Floquet protocol based on the use of light confined inside a waveguide. The boundary conditions imposed by the metallic surfaces of the waveguide allow a nonzero longitudinal component in the vector potential, which can couple to the component of the tunneling perpendicular to the TDBG plane. In the highfrequency regime, this protocol allows one to directly decrease the tunneling amplitude without breaking symmetries.

As in free space, the effect of the drive in a waveguide enters through a Peierls substitution to the hopping term in a real-space tight-binding Hamiltonian. In particular, the hopping term between two sites \mathbf{R} and \mathbf{R}' acquires the position-dependent phase $c_R^\dagger c_{R'} \to \exp(-i\int_R^{R'} dlA) c_R^\dagger c_{R'}$, where $c_{R'}$ and c_R^\dagger are the annihilation and creation operators. Assuming that the tight binding is defined in the x-y plane and the longitudinal vector potential $A(\mathbf{r},t) \approx A(t) \hat{e}_z$ is incident in the z direction and constant, $c_R^\dagger c_{R'} \to e^{-il_z A} c_R^\dagger c_{R'}$, with $l_z \equiv (\mathbf{R}' - \mathbf{R})_z$.

For TDBG, the time-dependent Hamiltonian in the continuum limit is given by

$$H_{ss'}(\mathbf{k}, \mathbf{x}, t) = \tau_u \otimes h_s(-\theta/2, \mathbf{k} - \kappa_-, t)$$

$$+ \tau_d \otimes h_{s'}(\theta/2, \mathbf{k} - \kappa_+, t)$$

$$+ \tau^+ \otimes \lambda^- \otimes T(\mathbf{x}, t) + \tau^- \otimes \lambda^+ \otimes T^{\dagger}(\mathbf{x}, t),$$
(16)

where

$$h_{s}(\theta, \boldsymbol{k}, t) = \begin{pmatrix} \Delta_{1} + \delta_{s}^{-} & \gamma_{0} f(R_{\theta} \boldsymbol{k}) & t_{s}(\boldsymbol{k}, t) \\ \gamma_{0} f^{*}(R_{\theta} \boldsymbol{k}) & \Delta_{1} + \delta_{s}^{+} & \\ t_{s}^{\dagger}(\boldsymbol{k}, t) & \Delta_{2} + \delta_{s}^{+} & \gamma_{0} f(R_{\theta} \boldsymbol{k}) \\ t_{s}^{\dagger}(\boldsymbol{k}, t) & \gamma_{0} f^{*}(R_{\theta} \boldsymbol{k}) & \Delta_{2} + \delta_{s}^{-} \end{pmatrix},$$

$$(17)$$

$$t_{+}(\boldsymbol{k},t) = \begin{pmatrix} -\gamma_{4} f(R_{\theta} \boldsymbol{k}) & -\gamma_{3} f^{*}(R_{\theta} \boldsymbol{k}) \\ \gamma_{1} & -\gamma_{4} f(R_{\theta} \boldsymbol{k}) \end{pmatrix} e^{-ia_{AB}A(t)}.$$
(18)

The tunneling sector also depends on the bilayer stacking configuration s. Finally, the interlayer hopping matrix acquires a time dependence according to

$$T(x,t) = \sum_{i=-1}^{1} e^{-iQ_i \cdot x} T_i(t),$$
 (19)

$$T_i = e^{-ia_{AA}A(t)}w_0\mathbb{1}_2 + e^{-ia_{AB}A(t)}w_1$$

$$\times \left[\cos\left(\frac{2\pi i}{3}\right)\sigma_1 + \sin\left(\frac{2\pi i}{3}\right)\sigma_2\right]. \tag{20}$$

The above Hamiltonian is obtained by performing the substitutions

$$\tau_{u,d} \otimes \lambda^{\pm} \otimes \sigma_i \to \tau_{u,d} \otimes \lambda^{\pm} \otimes \sigma_i e^{\mp i a_{AB} A(t)},$$
 (21a)

$$\tau^{\pm} \otimes \lambda^{\mp} \times \mathbb{1} \to \tau^{\pm} \otimes \lambda^{\mp} \times \mathbb{1} e^{\mp i a_{AA} A(t)},$$
 (21b)

$$\tau^{\pm} \otimes \lambda^{\mp} \times \sigma_{1,2} \to \tau^{\pm} \otimes \lambda^{\mp} \times \mathbb{1}e^{\mp ia_{AB}A(t)},$$
(21c)

as one can confirm when mapping the corresponding tight-binding hopping processes onto an effective single-particle Hamiltonian. Here $a_{AA,AB}$ describes the interlayer distance in AA and AB stacked bilayer graphene. The functional form of $T(\mathbf{x},t)$ implies that the coupling $\tau^\pm \otimes \lambda^\mp \times \sigma_{1,2}$ is dominant in AB regions and $\tau^\pm \otimes \lambda^\mp \times 1$ is dominant in AA regions. We have used this to get the approximate form in Eqs. (21b)

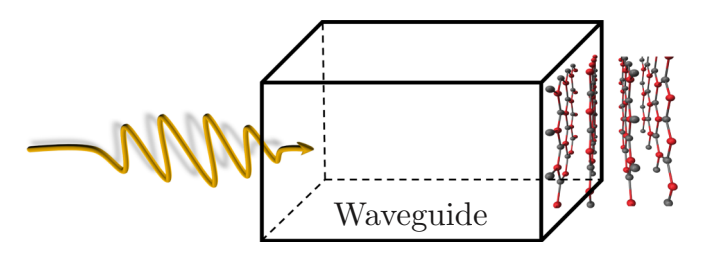


FIG. 10. Sketch of double bilayer graphene irradiated by circularly polarized light in a waveguide. The boundary condition imposed by the metallic walls allows for transverse modes in the electric field.

and (21c). This approximation is a simplification over the general position dependence of $T(x) \to T(x)e^{-ia(x,y)A}$, where the distance between layers would vary smoothly in space.

Specifically, we consider a transverse magnetic mode of light at the exit of a waveguide as shown in Fig. 10, which for a finite region in space can have the form $A \approx$ $A\cos(\Omega t)\hat{e}_z$ [63]. In the high-frequency regime, we obtain an effect Floquet Hamiltonian using a Van Vleck expansion to first order $H_{\text{eff}} \approx H_0 + \sum_{m \neq 0} [H_{-m}, H_m]/(2m\Omega)$, where $H_m = 1/T \int_0^T H(t)e^{-im\Omega t}$. The corrections of order $1/\Omega$ vanish if derivatives $\partial_i T(x,t)$ are neglected. This is justified because all derivatives in H_m and $m \neq 0$ appear with a prefactor $\gamma_{3,4}$ that is small and the terms $[H_{-m}, H_m]/(2m\Omega)$ are already suppressed by $1/\Omega$. In the small-angle regime, where T(x, t) varies slowly in real space, this approximation becomes even better because then the corrections that would arise have an additional small factor θ . Therefore, the leading correction is given by the averaged Hamiltonian H_0 , which shares the same structure of the static Hamiltonian with renormalized parameters

$$(w_1, \gamma_{1,3,4}) \to (w_1, \gamma_{1,3,4}) J_0(a_{AB}A),$$

 $w_0 \to w_0 J_0(a_{AA}A),$ (22)

where J_0 is the zeroth Bessel function of the first kind. Therefore, in the high-frequency regime, the interlayer couplings are suppressed by this type of electromagnetic field. This can lead to a renormalization of the bandwidth. In Fig. 11 we plot the quasienergies near the Floquet zone center along a

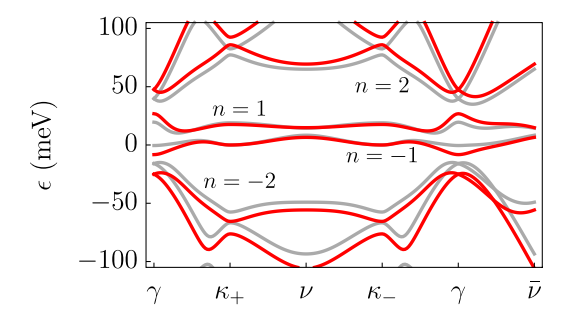


FIG. 11. Quasienergies along a high-symmetry path in the MBZ for AB/AB TDBG driven with light confined in a waveguide for $a_{AB}A \approx 0.136$. The gray lines correspond to the static energies. The index n labels the bands closest to the Floquet zone center.

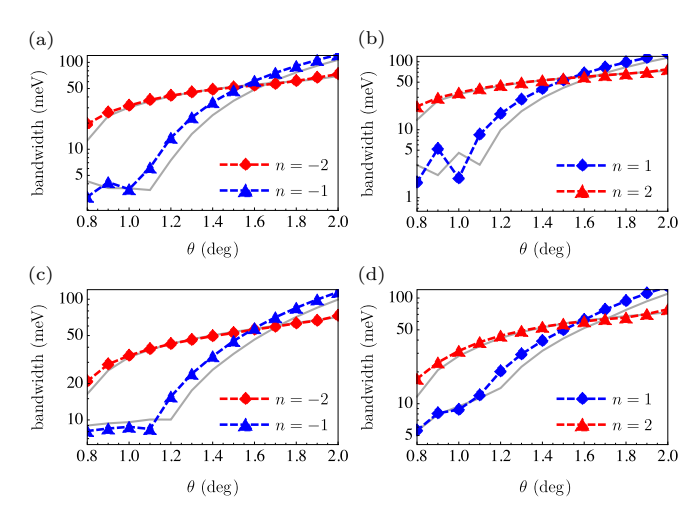


FIG. 12. Bandwidth of the four Floquet bands closest to the Floquet zone center as a function of the twist angle for (a) and (b) the case $\gamma_{3,4} = 0$ and (c) and (d) the case $\gamma_3 = 283$ meV and $\gamma_4 = 138$ meV. The drive parameters are $\Omega/W = 2$ and $a_{AB}A \approx 0.136$. The gray lines correspond to the static case.

high-symmetry path in the MBZ. The waveguide drive renormalized the bands, without breaking the symmetries of the static system. The renormalization of the bandwidth depends on the twist angle. In Fig. 12 we show the bandwidth of the four bands closest to the Floquet zone center as a function of the twist angle between the layers considering the effect of trigonal warping and particle-hole symmetry-breaking terms. These results suggest that dynamical bandwidth tuning could be achieved in TDBG samples without breaking the symmetries of the static system.

V. EXPERIMENTAL PARAMETER ESTIMATES

The laser drive parameters required to obtain the effects discussed here are accessible in experimental settings. The quasienergy gap closings for TDBG without applied static electric field were obtained for driving strengths $(e/\hbar)a_0A = ea_0E/(\hbar\Omega) \lesssim 0.06$. For the high frequency considered in the UV regime, $\hbar\Omega = 2W \approx 5350$ meV, a peak electric field $E\approx 9.5$ MV/cm leads to the required driving strength. A combination of a stronger electric field and lower driving frequency also could be considered. For example, to obtain Floquet flat bands, as shown in Fig. 9, we use $\hbar\Omega = 1.05W \approx 2809$ meV and driving strength $(e/\hbar)a_0A = ea_0E/(\hbar\Omega) \approx 0.3$, which can be obtained with a peak electric field $E\approx 25$ MV/cm. In graphene, laser pulses with peak electric fields of 30 MV/cm with near-IR frequencies have been employed to generate light-field-driven currents [98].

VI. CONCLUSION

We have studied twisted double bilayer graphene driven by circularly polarized light in free space and confined to a waveguide. For light propagating in free space, we demonstrated that TDBG in the AB/AB configuration with an applied static electric field perpendicular to the layers, the drive

permits valley-selective quasienergy gap engineering. The periodic drive also leads to a topological transition into a Chern insulating state due to the broken time-reversal symmetry. For TDBG in the AB/BA configuration, the driving protocol can lead to valley-selective engineering even in the absence of an applied electric field. Finally, we showed that stronger drives can generate Floquet flat bands. On the other hand, light confined to a waveguide allows us to dynamically tune the bandwidth of the Floquet zone-center bands without breaking the symmetries of the static system. Therefore, employing two complementary Floquet protocols, we showed that light-driven TDBG is a flexible system that could be used as a platform to generate valley-polarized currents.

Note added. Recently, related theoretical work was presented by Lu *et al.* in [99].

ACKNOWLEDGMENTS

This research was primarily supported by the National Science Foundation through the Center for Dynamics and Control of Materials: an NSF MRSEC under Cooperative Agreement No. DMR-1720595, with additional support from NSF Grant No. DMR-1949701.

APPENDIX: EFFECTIVE FLOQUET HAMILTONIAN IN THE INTERMEDIATE-FREQUENCY REGIME

For simplicity of discussion we will neglect the effects of trigonal warping for this Appendix. That is, the model Hamiltonian we consider is

$$H_{0,s} = \begin{pmatrix} h_{t,s}^{+} + \Delta_{1} & t_{s} & 0 & 0\\ t_{s}^{\dagger} & h_{b,s}^{+} + \Delta_{2} & T(\mathbf{r}) & 0\\ 0 & T^{\dagger}(\mathbf{r}) & h_{t,s}^{-} + \Delta_{3} & t_{s}\\ 0 & 0 & t_{s}^{\dagger} & h_{b,s}^{-} + \Delta_{4} \end{pmatrix},$$
(A1)

where $h_{l,s}^d = v_F[R(-d\theta/2)(k-\kappa_d)]\sigma_{xy} + \delta(\mathbb{1}-ls\sigma_3)$ is the Hamiltonian for graphene and the index $d=\pm$ labels the two graphene bilayers and $l=\pm$ (with + for t and – for b) labels the layers of each double layer. Furthermore, we distinguish between AB and BA stacking for the double layers via a term s that is $s=\pm$ for AB/BA stacking. Therefore, $\delta ls\sigma_3$ is a stacking- and layer-dependent gap and t is the interlayer hopping matrix for the top and bottom double layers with $t_s=t/2(\sigma_1-is\sigma_2)$. The term

$$T(\mathbf{r}) = \sum_{i=-1}^{1} e^{-i\mathbf{Q}_i \cdot \mathbf{r}} T_i, \tag{A2}$$

with

$$T_n = \omega' \mathbb{1}_2 + \omega \left[\cos \left(\frac{2\pi n}{3} \right) \sigma_1 + \sin \left(\frac{2\pi n}{3} \right) \sigma_2 \right],$$

describes the hopping between the two bilayers and captures the spatial dependence due to the mutual rotation. It depends on two coupling strengths ω and ω' that capture the effect that AB/BA and AA-type regions of the center twisted bilayer can have different lattice constants. Since the hopping

is dominated by hopping between adjacent layers, we neglect higher-order interlayer tunnelings. Finally, Δ_i describe a layer-dependent bias.

We introduce circularly polarized light by means of minimal substitution $p \to p + A/v_F$ with $A = A(\cos(\Omega t), \sin(\Omega))$. The Hamiltonian then becomes periodically time dependent H(t) = H(t+T) with period T and can be split as $H(t) = H_0 + V(t)$, where

$$V(t) = \begin{pmatrix} v^{+}(t) & 0 & 0 & 0\\ 0 & v^{+}(t) & 0 & 0\\ 0 & 0 & v^{-}(t) & 0\\ 0 & 0 & 0 & v^{-}(t) \end{pmatrix},$$
(A3)

with $v^{\pm}(t) = R(\mp \theta) A \sigma_{xy}$.

The time dependence makes a full treatment of the problem cumbersome, especially if one wants to build on the model and introduce additional complications such as disorder. Luckily, the time dependence can be reduced. This can either be done via a perturbative expansion or nonperturbatively by going to a rotating frame. A useful rotating frame of such a sort is implemented by a unitary transformation U(t) that fulfills U(T) = 1 because at stroboscopic times one may forget about the unitary transformation since it is unity. Naively, one may choose such a unitary transform that has the form $U(t) = \exp[-i \int dt V(t)]$. While this is useful and leads to good results, it is not the ideal choice for the problem at hand. This is because it can introduce mathematical artifacts such as an unphysical breaking of rotational symmetry like in the case of graphene [43,62]. For our case we therefore employ a better choice that was introduced in [62] and split the time-dependent part of the Hamiltonian as

$$V_{1}(t) = A\cos(\omega t) \begin{pmatrix} \sigma_{1}^{\theta/2} & 0 & 0 & 0\\ 0 & \sigma_{1}^{\theta/2} & 0 & 0\\ 0 & 0 & \sigma_{1}^{-\theta/2} & 0\\ 0 & 0 & 0 & \sigma_{1}^{-\theta/2} \end{pmatrix}, \quad (A4)$$

$$V_{2}(t) = A\sin(\omega t) \begin{pmatrix} \sigma_{2}^{\theta/2} & 0 & 0 & 0\\ 0 & \sigma_{2}^{\theta/2} & 0 & 0\\ 0 & 0 & \sigma_{2}^{-\theta/2} & 0\\ 0 & 0 & 0 & \sigma_{2}^{-\theta/2} \end{pmatrix},$$

where the rotated Pauli matrices $\sigma_i^{\theta/2}$ given by $\sigma_i^{\theta/2} = e^{i/4\theta\sigma_3}\sigma_i e^{-i/4\theta\sigma_3}$ were introduced as a convenient shorthand. The unitary transformation we use now is given as

$$U(t) = \exp\left(-i\int dt V_1(t)\right) \exp\left(-i\int dt V_2(t)\right).$$
 (A5)

This choice is useful because it preserves rotational invariance of the dispersion relation after a time average over one period if the interlayer couplings are neglected as seen in [62] and leads to an improvement over more conventional high-frequency expansions.

If we apply this unitary transformation to the Schrödinger equation $i\partial_t \psi = [H_0 + V(t)]\psi$ and take an average over one

period, we arrive at the effective Hamiltonian

$$H_{F,s} = R^{\dagger} \begin{pmatrix} \tilde{h}_{t,s}^{+} + \Delta_{1} & \tilde{t}_{s} & 0 & 0\\ \tilde{t}_{s}^{\dagger} & \tilde{h}_{b,s}^{+} + \Delta_{2} & \tilde{T}(\mathbf{r}) & 0\\ 0 & \tilde{T}^{\dagger}(\mathbf{r}) & \tilde{h}_{t,s}^{-} + \Delta_{3} & \tilde{t}_{s}\\ 0 & 0 & \tilde{t}_{s}^{\dagger} & \tilde{h}_{b,s}^{-} + \Delta_{4} \end{pmatrix} R,$$
(A6)

where R is a unitary transformation given as

$$R = \begin{pmatrix} R_{+} & 0 & 0 & 0\\ 0 & R_{+} & 0 & 0\\ 0 & 0 & R_{-} & 0\\ 0 & 0 & 0 & R_{-} \end{pmatrix}, \tag{A7}$$

with

$$R_{\pm} = \exp\bigg(-rac{i}{2}\sigma_2^{\pm heta/2} ilde{A}\bigg),$$

which includes a rotation around the y axis in pseudospin space with angle $\tilde{A} = \frac{2A}{\Omega}$. In this rotated space we find that the Hamiltonian for a single graphene layer is modified as

$$\tilde{h}_{l,s}^{d} = \tilde{v}_{F}[R(-d \theta/2)k]\sigma_{xy} + \delta(\mathbb{1} - lsJ_{0}(\sqrt{2}\tilde{A})\sigma_{3}) - \tilde{\Delta}\sigma_{3},$$
(A8)

- [1] R. Bistritzer and A. H. MacDonald, Proc. Natl. Acad. Sci. U.S.A. 108, 12233 (2011).
- [2] J. M. B. Lopes dos Santos, N. M. R. Peres, and A. H. Castro Neto, Phys. Rev. B 86, 155449 (2012).
- [3] E. Suárez Morell, J. D. Correa, P. Vargas, M. Pacheco, and Z. Barticevic, Phys. Rev. B 82, 121407(R) (2010).
- [4] Y. Cao, V. Fatemi, A. Demir, S. Fang, S. L. Tomarken, J. Y. Luo, J. D. Sanchez-Yamagishi, K. Watanabe, T. Taniguchi, E. Kaxiras, R. C. Ashoori, and P. Jarillo-Herrero, Nature (London) 556, 80 (2018).
- [5] Y. Cao, V. Fatemi, S. Fang, K. Watanabe, T. Taniguchi, E. Kaxiras, and P. Jarillo-Herrero, Nature (London) 556, 43 (2018).
- [6] E. Codecido, Q. Wang, R. Koester, S. Che, H. Tian, R. Lv, S. Tran, K. Watanabe, T. Taniguchi, F. Zhang, M. Bockrath, and C. N. Lau, Sci. Adv. 5, eaaw9770 (2019).
- [7] D. Wong, K. P. Nuckolls, M. Oh, B. Lian, Y. Xie, S. Jeon, K. Watanabe, T. Taniguchi, B. A. Bernevig, and A. Yazdani, Nature (London) 582, 198 (2020).
- [8] X. Lu, P. Stepanov, W. Yang, M. Xie, M. A. Aamir, I. Das, C. Urgell, K. Watanabe, T. Taniguchi, G. Zhang, A. Bachtold, A. H. MacDonald, and D. K. Efetov, Nature (London) 574, 653 (2019).
- [9] A. L. Sharpe, E. J. Fox, A. W. Barnard, J. Finney, K. Watanabe, T. Taniguchi, M. A. Kastner, and D. Goldhaber-Gordon, Science 365, 605 (2019).
- [10] K. Seo, V. N. Kotov, and B. Uchoa, Phys. Rev. Lett. 122, 246402 (2019).
- [11] K. Tran, G. Moody, F. Wu, X. Lu, J. Choi, K. Kim, A. Rai, D. A. Sanchez, J. Quan, A. Singh, J. Embley, A. Zepeda, M. Campbell, T. Autry, T. Taniguchi, K. Watanabe, N. Lu, S. K. Banerjee, K. L. Silverman, S. Kim, E. Tutuc, L. Yang, A. H. MacDonald, and X. Li, Nature (London) 567, 71 (2019).

where we find that the layer- and stacking-dependent gap $ls\sigma_3 \rightarrow lsJ_0(\sqrt{2}\tilde{A})$ has been suppressed by $J_0(\sqrt{2}\tilde{A})$, where J_i are Bessel functions of the first kind. The Fermi velocity is lowered to $v_F \rightarrow \tilde{v}_F = J_0(\tilde{A})v_F$ and a new stacking- and layer-independent gap $\tilde{\Delta} = A\frac{J_1(\frac{2\sqrt{2}\tilde{A}}{\Omega})}{\sqrt{2}}$ has been introduced. For the interlayer couplings in the two double layers we find $t_s = \tilde{t}/2(\sigma_1 - is\sigma_2)$, with merely the strength renormalized to $t \rightarrow \tilde{t} = tJ_0(\tilde{A})$. The position-dependent interlayer coupling for the two center graphene layers changes to

$$\tilde{T}(\mathbf{r}) = \sum_{i=-1}^{1} e^{-i\mathbf{Q}_i \cdot \mathbf{r}} \{ \tilde{T}_i + \omega_{\theta/2}'' [\sin(\theta/2) \mathbb{1}_2 - i\cos(\theta/2) \sigma_3] \},$$

with

$$\tilde{T}_n = \omega' \mathbb{1}_2 + \tilde{\omega} \left[\cos \left(\frac{2\pi n}{3} \right) \sigma_1 + \sin \left(\frac{2\pi n}{3} \right) \sigma_2 \right], \quad (A9)$$

where the coupling $\omega \to \tilde{\omega} = J_0(\tilde{A})\omega$ has been renormalized and a new angle-dependent coupling $\omega''_{\theta/2} = \sin(\theta/2)[J_0(\sqrt{2}\tilde{A}) - 1]\omega'$ has been introduced.

- [12] K. L. Seyler, P. Rivera, H. Yu, N. P. Wilson, E. L. Ray, D. G. Mandrus, J. Yan, W. Yao, and X. Xu, Nature (London) 567, 66 (2019).
- [13] E. M. Alexeev, D. A. Ruiz-Tijerina, M. Danovich, M. J. Hamer, D. J. Terry, P. K. Nayak, S. Ahn, S. Pak, J. Lee, J. I. Sohn, M. R. Molas, M. Koperski, K. Watanabe, T. Taniguchi, K. S. Novoselov, R. V. Gorbachev, H. S. Shin, V. I. Fal'ko, and A. I. Tartakovskii, Nature (London) 567, 81 (2019).
- [14] Y. Cao, D. Rodan-Legrain, O. Rubies-Bigorda, J. M. Park, K. Watanabe, T. Taniguchi, and P. Jarillo-Herrero, Nature (London) 583, 215 (2020).
- [15] N. R. Chebrolu, B. L. Chittari, and J. Jung, Phys. Rev. B 99, 235417 (2019).
- [16] M. Koshino, Phys. Rev. B 99, 235406 (2019).
- [17] J. Y. Lee, E. Khalaf, S. Liu, X. Liu, Z. Hao, P. Kim, and A. Vishwanath, Nat. Commun. 10, 5333 (2019).
- [18] F. Haddadi, Q. Wu, A. J. Kruchkov, and O. V. Yazyev, Nano Lett. 20, 2410 (2020).
- [19] F. J. Culchac, R. R. Del Grande, R. B. Capaz, L. Chico, and E. S. Morell, Nanoscale 12, 5014 (2020).
- [20] Y.-H. Zhang, D. Mao, Y. Cao, P. Jarillo-Herrero, and T. Senthil, Phys. Rev. B 99, 075127 (2019).
- [21] M. Yankowitz, S. Chen, H. Polshyn, Y. Zhang, K. Watanabe, T. Taniguchi, D. Graf, A. F. Young, and C. R. Dean, Science 363, 1059 (2019).
- [22] S. Carr, S. Fang, P. Jarillo-Herrero, and E. Kaxiras, Phys. Rev. B **98**, 085144 (2018).
- [23] B. L. Chittari, N. Leconte, S. Javvaji, and J. Jung, Electron. Struct. 1, 015001 (2018).
- [24] M. Yankowitz, J. Jung, E. Laksono, N. Leconte, B. L. Chittari, K. Watanabe, T. Taniguchi, S. Adam, D. Graf, and C. R. Dean, Nature (London) 557, 404 (2018).
- [25] F. Wu, T. Lovorn, and A. H. MacDonald, Phys. Rev. Lett. 118, 147401 (2017).

- [26] H. Yu, G.-B. Liu, J. Tang, X. Xu, and W. Yao, Sci. Adv. 3, e1701696 (2017).
- [27] T. Oka and H. Aoki, Phys. Rev. B 79, 081406(R) (2009).
- [28] A. Eckardt and E. Anisimovas, New J. Phys. 17, 093039 (2015).
- [29] S. Blanes, F. Casas, J. Oteo, and J. Ros, Phys. Rep. 470, 151 (2009).
- [30] E. Fel'dman, Phys. Lett. A **104**, 479 (1984).
- [31] W. Magnus, Commun. Pure Appl. Math. 7, 649 (1954).
- [32] D. A. Abanin, W. De Roeck, W. W. Ho, and F. Huveneers, Phys. Rev. B 95, 014112 (2017).
- [33] M. Bukov, L. D'Alessio, and A. Polkovnikov, Adv. Phys. 64, 139 (2015).
- [34] S. Rahav, I. Gilary, and S. Fishman, Phys. Rev. A 68, 013820 (2003).
- [35] N. Goldman and J. Dalibard, Phys. Rev. X 4, 031027 (2014).
- [36] A. P. Itin and M. I. Katsnelson, Phys. Rev. Lett. 115, 075301 (2015).
- [37] T. Mikami, S. Kitamura, K. Yasuda, N. Tsuji, T. Oka, and H. Aoki, Phys. Rev. B 93, 144307 (2016).
- [38] P. Mohan, R. Saxena, A. Kundu, and S. Rao, Phys. Rev. B 94, 235419 (2016).
- [39] M. Bukov, M. Kolodrubetz, and A. Polkovnikov, Phys. Rev. Lett. 116, 125301 (2016).
- [40] M. M. Maricq, Phys. Rev. B 25, 6622 (1982).
- [41] M. Vogl, P. Laurell, A. D. Barr, and G. A. Fiete, Phys. Rev. X 9, 021037 (2019).
- [42] M. Vogl, P. Laurell, A. D. Barr, and G. A. Fiete, Phys. Rev. A 100, 012132 (2019).
- [43] M. Vogl, M. Rodriguez-Vega, and G. A. Fiete, Phys. Rev. B **101**, 024303 (2020).
- [44] M. Rodriguez-Vega, M. Lentz, and B. Seradjeh, New J. Phys. **20**, 093022 (2018).
- [45] H. Martiskainen and N. Moiseyev, Phys. Rev. A 91, 023416 (2015).
- [46] G. Rigolin, G. Ortiz, and V. H. Ponce, Phys. Rev. A 78, 052508 (2008).
- [47] M. Weinberg, C. Ölschläger, C. Sträter, S. Prelle, A. Eckardt, K. Sengstock, and J. Simonet, Phys. Rev. A 92, 043621 (2015).
- [48] A. Verdeny, A. Mielke, and F. Mintert, Phys. Rev. Lett. 111, 175301 (2013).
- [49] J. W. McIver, B. Schulte, F.-U. Stein, T. Matsuyama, G. Jotzu, G. Meier, and A. Cavalleri, Nat. Phys. 16, 38 (2020).
- [50] V. G. Ibarra-Sierra, J. C. Sandoval-Santana, A. Kunold, and G. G. Naumis, Phys. Rev. B 100, 125302 (2019).
- [51] W.-R. Lee and W.-K. Tse, Phys. Rev. B 95, 201411(R) (2017).
- [52] M. Rodriguez-Vega and B. Seradjeh, Phys. Rev. Lett. **121**, 036402 (2018).
- [53] M. Rodriguez-Vega, H. A. Fertig, and B. Seradjeh, Phys. Rev. B 98, 041113(R) (2018).
- [54] M. Rodriguez-Vega, A. Kumar, and B. Seradjeh, Phys. Rev. B 100, 085138 (2019).
- [55] L. Privitera, A. Russomanno, R. Citro, and G. E. Santoro, Phys. Rev. Lett. 120, 106601 (2018).
- [56] J. C. Sandoval-Santana, V. G. Ibarra-Sierra, J. L. Cardoso, A. Kunold, P. Roman-Taboada, and G. Naumis, Ann. Phys. (Berlin) 531, 1900035 (2019).
- [57] P. Kumar, T. M. Herath, V. Apalkov, and M. I. Stockman, Ultrafast valley polarization in bilayer graphene, arXiv:2007.13480.

- [58] P. Kumar, T. M. Herath, V. Apalkov, and M. I. Stockman, Bilayer graphene in strong ultrafast laser fields, arXiv:2004.09732.
- [59] G. E. Topp, G. Jotzu, J. W. McIver, L. Xian, A. Rubio, and M. A. Sentef, Phys. Rev. Research 1, 023031 (2019).
- [60] Y. Li, H. A. Fertig, and B. Seradjeh, Floquet-engineered topological flat bands in irradiated twisted bilayer graphene, arXiv:1910.04711.
- [61] O. Katz, G. Refael, and N. H. Lindner, Floquet flat-band engineering of twisted bilayer graphene, arXiv:1910.13510.
- [62] M. Vogl, M. Rodriguez-Vega, and G. A. Fiete, Phys. Rev. B 101, 235411 (2020).
- [63] M. Vogl, M. Rodriguez-Vega, and G. A. Fiete, Phys. Rev. B 101, 241408(R) (2020).
- [64] D. S. L. Abergel and T. Chakraborty, Appl. Phys. Lett. 95, 062107 (2009).
- [65] F. Qi and G. Jin, J. Appl. Phys. 115, 173701 (2014).
- [66] A. Kundu, H. A. Fertig, and B. Seradjeh, Phys. Rev. Lett. 116, 016802 (2016).
- [67] Á. Jiménez-Galán, R. E. F. Silva, O. Smirnova, and M. Ivanov, arXiv:1910.07398.
- [68] F. Langer, C. P. Schmid, S. Schlauderer, M. Gmitra, J. Fabian, P. Nagler, C. Schüller, T. Korn, P. G. Hawkins, J. T. Steiner, U. Huttner, S. W. Koch, M. Kira, and R. Huber, Nature (London) 557, 76 (2018).
- [69] D. Shin, H. Hübener, U. De Giovannini, H. Jin, A. Rubio, and N. Park, Nat. Commun. 9, 638 (2018).
- [70] J. R. Schaibley, H. Yu, G. Clark, P. Rivera, J. S. Ross, K. L. Seyler, W. Yao, and X. Xu, Nat. Rev. Mater. 1, 16055 (2016).
- [71] S. A. Vitale, D. Nezich, J. O. Varghese, P. Kim, N. Gedik, P. Jarillo-Herrero, D. Xiao, and M. Rothschild, Small 14, 1801483 (2018).
- [72] D. Xiao, W. Yao, and Q. Niu, Phys. Rev. Lett. 99, 236809 (2007).
- [73] W. Yao, D. Xiao, and Q. Niu, Phys. Rev. B 77, 235406 (2008).
- [74] D. Xiao, G.-B. Liu, W. Feng, X. Xu, and W. Yao, Phys. Rev. Lett. 108, 196802 (2012).
- [75] X. Li, F. Zhang, and Q. Niu, Phys. Rev. Lett. 110, 066803 (2013).
- [76] K. F. Mak, K. L. McGill, J. Park, and P. L. McEuen, Science 344, 1489 (2014).
- [77] R. V. Gorbachev, J. C. W. Song, G. L. Yu, A. V. Kretinin, F. Withers, Y. Cao, A. Mishchenko, I. V. Grigorieva, K. S. Novoselov, L. S. Levitov, and A. K. Geim, Science 346, 448 (2014).
- [78] E. J. Sie, J. W. McIver, Y.-H. Lee, L. Fu, J. Kong, and N. Gedik, Nat. Mater. 14, 290 (2015).
- [79] E. J. Sie, C. H. Lui, Y.-H. Lee, L. Fu, J. Kong, and N. Gedik, Science 355, 1066 (2017).
- [80] M. Sui, G. Chen, L. Ma, W.-Y. Shan, D. Tian, K. Watanabe, T. Taniguchi, X. Jin, W. Yao, D. Xiao, and Y. Zhang, Nat. Phys. 11, 1027 (2015).
- [81] Y. Shimazaki, M. Yamamoto, I. V. Borzenets, K. Watanabe, T. Taniguchi, and S. Tarucha, Nat. Phys. 11, 1032 (2015).
- [82] J. Jung and A. H. MacDonald, Phys. Rev. B 89, 035405 (2014).
- [83] N. N. T. Nam and M. Koshino, Phys. Rev. B 96, 075311 (2017).
- [84] M. Fleischmann, R. Gupta, S. Sharma, and S. Shallcross, Moiré quantum well states in tiny angle two dimensional semi-conductors, arXiv:1901.04679.

- [85] L. Balents, SciPost Phys. 7, 48 (2019).
- [86] J. Li, D. Golez, G. Mazza, A. J. Millis, A. Georges, and M. Eckstein, Phys. Rev. B 101, 205140 (2020).
- [87] H. Sambe, Phys. Rev. A 7, 2203 (1973).
- [88] P. M. Perez-Piskunow, L. E. F. Foa Torres, and G. Usaj, Phys. Rev. A 91, 043625 (2015).
- [89] A. Kumar, M. Rodriguez-Vega, T. Pereg-Barnea, and B. Seradjeh, Phys. Rev. B 101, 174314 (2020).
- [90] M. S. Rudner, N. H. Lindner, E. Berg, and M. Levin, Phys. Rev. X 3, 031005 (2013).
- [91] J. Yan, M.-H. Kim, J. A. Elle, A. B. Sushkov, G. S. Jenkins, H. M. Milchberg, M. S. Fuhrer, and H. D. Drew, Nat. Nanotechnol. 7, 472 (2012).
- [92] M.-H. Kim, J. Yan, R. J. Suess, T. E. Murphy, M. S. Fuhrer, and H. D. Drew, Phys. Rev. Lett. 110, 247402 (2013).
- [93] S. A. Weidinger and M. Knap, Sci. Rep. 7, 45382 (2017).

- [94] H. Dehghani, T. Oka, and A. Mitra, Phys. Rev. B 90, 195429 (2014).
- [95] S. A. Sato, J. W. McIver, M. Nuske, P. Tang, G. Jotzu, B. Schulte, H. Hübener, U. De Giovannini, L. Mathey, M. A. Sentef, A. Cavalleri, and A. Rubio, Phys. Rev. B 99, 214302 (2019).
- [96] S. A. Sato, P. Tang, M. A. Sentef, U. D. Giovannini, H. Hübener, and A. Rubio, New J. Phys. 21, 093005 (2019).
- [97] S. A. Sato, U. D. Giovannini, S. Aeschlimann, I. Gierz, H. Hübener, and A. Rubio, Floquet states in dissipative open quantum systems, arXiv:1912.03176.
- [98] T. Higuchi, C. Heide, K. Ullmann, H. B. Weber, and P. Hommelhoff, Nature (London) 550, 224 (2017).
- [99] M. Lu, J. Zeng, H. Liu, J.-H. Gao, and X. C. Xie, Valley-selective Floquet Chern flat bands in twisted multilayer graphene, arXiv:2007.15489.